

# Study on Vibration Compaction Energy of Basement Material

Hao Zhou <sup>1,\*</sup>, Yongjian Guo <sup>2</sup>, Qiang Xu <sup>1</sup>, Guixia Zhang <sup>3</sup> and Zhen Wang <sup>1</sup><sup>1</sup> School of Transportation Engineering, Shandong Jianzhu University, Jinan 250101, China<sup>2</sup> Qingdao Conson Second Jiaozhou Bay Subsea Tunnel Co., Ltd., Qingdao 266071, China<sup>3</sup> Shandong Institute of Highway Technican, Jinan 253032, China

\* Correspondence: zhouhao@sdjzu.edu.cn

**Abstract:** In order to confirm the vibrate compaction energy, the indoor vibration compaction was conducted. Indoor vibration compactor was used to compact skeleton dense cement stabilized aggregate. The acceleration and displacement of the indenter and compaction pressure during the compaction process were measured. The bounce model and the hysteresis curve based on measurement parameters were used to calculate the compaction energy. Three vibration compaction energy were affirmed as: energy of the machinery itself ( $E_{self}$ ), energy transmitted from machinery to compacted material ( $E_t$ ) and energy stored by compacted materials ( $E_s$ ). The energy  $E_{self}$  was about 40 J (joule). During each compaction process, energy  $E_t$  was only 1–1.8 J. In a one-minute compaction process, 2500 J of energy would be transmitted, but only 38 J could be stored by the compacted material.

**Keywords:** hysteresis curve; mechanical energy; transmitted energy; stored energy



**Citation:** Zhou, H.; Guo, Y.; Xu, Q.; Zhang, G.; Wang, Z. Study on Vibration Compaction Energy of Basement Material. *Coatings* **2022**, *12*, 1495. <https://doi.org/10.3390/coatings12101495>

Academic Editors: Michał Kulka and Alan Hase

Received: 30 June 2022

Accepted: 4 October 2022

Published: 7 October 2022

**Publisher's Note:** MDPI stays neutral with regard to jurisdictional claims in published maps and institutional affiliations.



**Copyright:** © 2022 by the authors. Licensee MDPI, Basel, Switzerland. This article is an open access article distributed under the terms and conditions of the Creative Commons Attribution (CC BY) license (<https://creativecommons.org/licenses/by/4.0/>).

## 1. Introduction

In the compaction process, the compact machine performs the work to overcome the internal friction between the material grain that is being compacted [1,2]. Compaction energy [3] is an important parameter of vibratory compaction [4,5]. The energy is generated in the motor and delivered to the compaction machine. Subsequently, a portion of the energy is transmitted to the ground when the compaction machine makes contact with the ground. As a result of compaction energy, ground deformation, including elastic deformation and plastic deformation [6,7], can occur. Once elastic deformation is accumulated, elastic it can be recovered, and the compaction effect [8] can be observed. Therefore, only a portion of the transmitted energy can be stored to enable plastic deformation. For the compaction process, three types of compaction energy are present: the energy within the machinery itself ( $E_{self}$ ), the energy transmitted from the machinery to the compacted material ( $E_t$ ), and the energy stored by the compacted materials ( $E_s$ ). The energy of the proctor [9] compaction and impact [10,11] compaction are fixed before each compaction process and the motor does not operate during the compaction process. Therefore, the  $E_s$  and  $E_t$  are equal and can be described by simple physical methods (proctor compaction and impact compaction).

Vibration compaction is more complicated [8,12], and the mechanical energy  $E_{self}$  frequently changes. Various models and methods have been used to analyze vibrational compaction energy, including kinetic models and integral algorithms [13]. The hysteresis curve is used to describe the vibration-compaction influence and energy dissipation of compacted material. The opening degree and the area of the hysteresis loops was used to calculate the compaction-energy law based on the hysteresis-loop study of frozen soil [14]. Furthermore, Bouc–Wen hysteresis modeling offers a versatile approach to describing various characteristics of hysteretic behavior [15].

Yan-feng Li calculated the compaction mechanical energy  $E_{self}$  using a mechanical model. By using a compaction-pressure sensor and theoretical derivation, Zhou-yang Cao measured the compaction-roller pressure and computed the work the roller performed to

compact the road material [16]. Liu [17] used unit-compaction energy (UCE), including unit-volume compaction energy (UVCE) and unit-area compaction energy (UACE), to evaluate the compaction capacity of vibrating machinery. The control criteria of the UVCE and UACE were established based on the density model, the laboratory-compaction-experiment shear-strength model, and the analysis of the mechanical model. The force and energy of the compaction were analyzed. The main calculation formula was as follows:

$$P = W + F \sin \omega t \quad (1)$$

$$E = WA(1 + \sin \varphi) + \frac{1}{2}FA \left[ \cos \varphi + \left( \varphi + \frac{\pi}{2} \right) \sin \varphi \right] \quad (2)$$

$$E_{0,1} = E \cdot N \cdot \frac{t}{T} \cdot \frac{1}{BHL} = E \cdot N \cdot \frac{l}{v} \cdot f \cdot \frac{1}{BHL} = 2A \left( W + \frac{\pi F}{4} \right) \frac{Nf}{BHv} \quad (3)$$

$$E_{0,2}(n) = E \cdot \frac{t}{T} \cdot \frac{1}{BL} \delta(h) = 2A \left( W + \frac{1}{4}F\pi \right) \cdot \frac{f}{Bv} \delta(h) \quad (4)$$

$P$ —radial load of the vibrating wheels (N);

$W$ —eccentric excitation frequency (rad/s);

$F$ —vertical-excitation-force amplitude due to the rotating eccentric (N);

$\omega$ —eccentric excitation frequency (rad/s);

$\varphi$ —phase difference between vertical exciting force and drum displacement ( $^{\circ}$ );

$E$ —compaction energy in a vibrating cycle (J);

$E_{0,1}$ —value of UVCE ( $\text{J}/\text{m}^3$ );

$E_{0,2}$ —value of UACE ( $\text{J}/\text{m}^3$ );

$B$ —drum width (m);

$H$ —lift thickness (m);

$L$ —compacted length (m);

$v$ —roller velocity (m/s).

We studied the energy exchange during the compaction process by calculating the energy carried by the vibration signal of the vibrating wheel [18]. The energy exchange in the compaction process was reflected by calculating the energy carried by the vibration signal of the vibrating wheel, after which the compaction degree of the filler was evaluated [19].

These studies primarily focused on the energy  $E_{self}$  and  $E_t$ . The energy of the compaction machine and the energy transmitted from the machine to the pavement can be accurately calculated. Further research should focus on the energy  $E_s$  and the systematic vibration-compaction energy. Some researchers studied the compaction of pavement materials through the compactor–pavement-material coupling model [20,21]. Through the coupling model, the effects of the compaction machine and the modulus [22] of the compacted materials can be analyzed. Furthermore, the mechanical-compaction work [23] can be extended.

In this research, the machine–soil pressure and indenter displacement were measured. In addition, the three sources of vibration compaction energy were identified and calculated based on the indoor compaction experiment and bounce model.

## 2. Materials and Methodology

### 2.1. Materials

Skeleton-dense cement stabilized aggregate was used in this experiment. Limestone was used as aggregate. The grade of cement stabilized skeleton-dense aggregate, which indicated that the cumulative pass rate of different sieves varied. They were tested according to *Test Methods of Aggregate for Highway Engineering (JTG E42—2005)* and the result is shown in Figure 1. The properties of cement, including the cement fineness, setting time, and strength of cement mortar were verified to identify the performance of cement. These properties met the *Technical Guidelines for Construction of Highway Roadbases (JTGT F20-2015)* and were tested according to *Test Methods of cement and cement concrete of Highway Engineering (JTG 3420-2020)*. As presented in Table 1, the cement dosage was 5%.

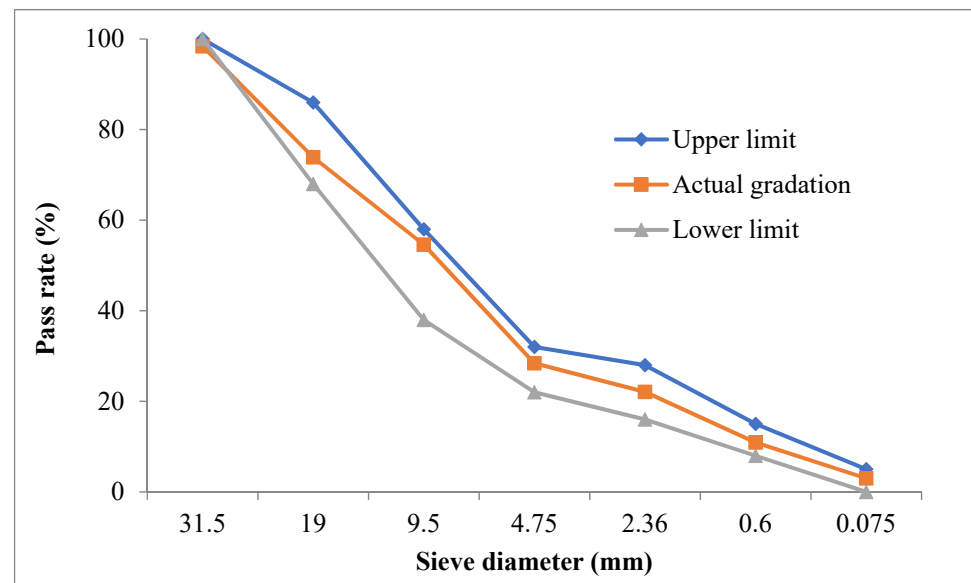


Figure 1. Grade of aggregate.

Table 1. Properties of cement.

Index	Residue (%) (80 $\mu$ m)	Initial Setting Time	Final Setting Time	3D Strength (MPa)	
				Compression	Flexural
cement	7.1	3 h 12 min	6 h 53 min	20.2	4.7

## 2.2. Methodology

### 2.2.1. Indoor Vibration Compaction

An indoor vibration compactor [24,25] was used during the compaction experiment, with the main structure illustrated in Figure 2. The electric motor of compaction equipment performs the work and energy is transported to the eccentric block. Therefore, the eccentric block drives the vibration-compaction instrument and vibrates up and down. The compaction energy is transmitted to compacted material through the indenter during the up-down vibration process and the material in the barrel is compacted. Indenter acceleration and displacement during the compaction process can be measured to determine the pressure between the indenter and compacted skeleton-dense cement stabilized aggregate.

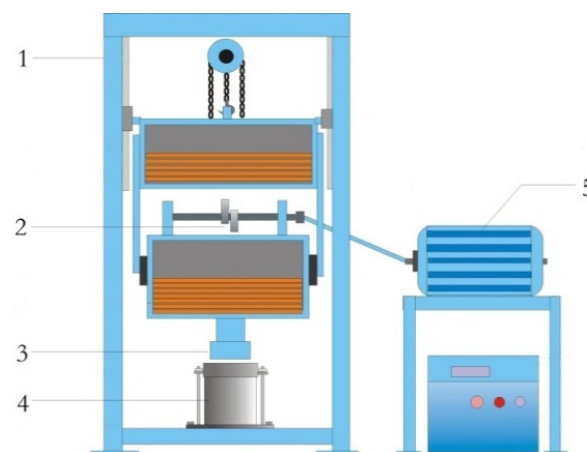


Figure 2. Indoor vibration-compaction mechanic structure. 1—Mechanics frame; 2—eccentric block; 3—indenter; 4—compaction barrels; 5—electric motor.

2.2.2. Self-Energy of the Machinery ( $E_{self}$ )

According to the Lawson Haosen’s mechanical model, the compaction force can be calculated as follows:

$$F_0 = Me\omega^2 \tag{5}$$

$$F = F_0 \sin \varphi$$

$F$ —excitation force (N);

$M$ —quality distribution on the indenter and counterweight (kg);

$e$ —vibratory-roller eccentricity (mm);

$\omega$ —angle between eccentric block and horizontal direction (deg).

The vibratory indenter jumps off the ground if the compaction force  $F$  is greater than roller gravity  $Mg$ . The equations of vibratory indenter and counterweight are as follows:

$$m_2x_2 = -Mg + Me \ddot{\omega}^2 \sin(\varphi_0 + \omega t) \tag{6}$$

$m_2$ —lower structure;

$g$ —acceleration of gravity ( $9.8 \text{ m/s}^2$ );

$\varphi_0$ —critical angle of structure taking off ground (deg).

$$\begin{cases} \dot{x}_2|_{t0} = 0 \\ x_2|_{t0} = 0 \end{cases}$$

so

$$\ddot{X} = -\frac{Mg}{m_2} \left( 1 - \cos \omega t + \sqrt{A^2 - 1} \sin t \right)$$

$$\dot{X} = \left[ -\omega t + \sin \varphi t + \sqrt{A^2 - 1}(1 - \cos \omega t) \right] \frac{g}{\omega} \frac{M}{m_2}$$

$$X = \left[ -\frac{1}{2}(\omega t)^2 - \cos \omega t + \sqrt{A^2 - 1}(\omega t - \sin \omega t) \right] \frac{g}{\omega} \frac{M}{m_2} + C_2 \tag{7}$$

According to the initial conditions,

$$x_2|_{t0} = 0$$

The indenter speed when the indenter is in contact with compacted pavement material can be calculated as:

$$V_a = \dot{X}_2(\varphi'_a) = \left[ -\varphi' + \sin \varphi' + \sqrt{A^2 - 1}(1 - \cos \varphi') \right] \frac{g}{\omega} \frac{M}{m_2} \tag{8}$$

$$A = \frac{F_0}{Mg}$$

$X$ —displacement of compaction machinery (m);

$\dot{X}$ —velocity of compaction machinery (m/s);

$\ddot{X}$ —acceleration of compaction machinery ( $\text{m/s}^2$ ).

When the vibratory roller hits the pavement surface, the indenter receives three kinds of energy: kinetic energy ( $E_v$ ), potential energy ( $E_p$ ), and impact energy ( $E_i$ ), which can be computed as:

$$E = E_v + E_p + E_i \tag{9}$$

$$E_v = \frac{1}{2}m_2v_a^2 \tag{10}$$

$$E_p = M \cdot g \cdot S_e \tag{11}$$

$$E_i = |v_a| \cdot M_e \cdot \omega \cdot \cos \varphi_a \tag{12}$$

$E$ —total energy of machine when it enters contact with ground;

$E_v$ —kinetic energy of machine when it enters contact with ground;  
 $E_p$ —potential energy of machine when it enters contact with ground;  
 $E_i$ —impact energy of machine when it enters contact with ground;  
 $S_e$ —ground settlement when it enters contact with ground;  
 $v_a$ —machine velocity when it enters contact with ground.

### 2.2.3. Transmitted Energy from Machinery to Compacted Material ( $E_t$ )

During the vibration-compaction process, the transmitted energy from the compaction machine to compacted material can be calculated [26] by the compaction pressure and displacement (Figure 3). The displacement-force curve is called the hysteresis curve, where the curve area represents the transmitted energy from compaction machine to compacted material. The pressure force and displacement can be tested by the pressure sensor and displacement sensor.

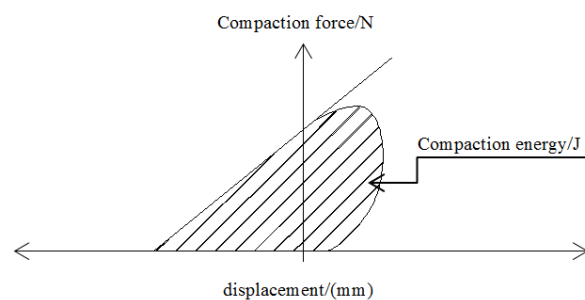


**Figure 3.** Vibration-compaction-energy-calculation diagram.

The compactor acceleration, displacement, and material pressure during the compaction process were measured by respective sensors. The pressure sensor was installed in the compaction barrel and the vibratory compactor and compaction barrel height were fixed. The final density was slightly lower than normal specimens as the actual specimen's height was about 7 cm rather than the standard 15 cm. The structure graph was shown in Figure 4. The compaction-pressure-displacement curve was drawn, where the curve area represented the compaction energy " $E_t$ " of one compaction cycle. Typical compaction signals of different compaction stages were studied.

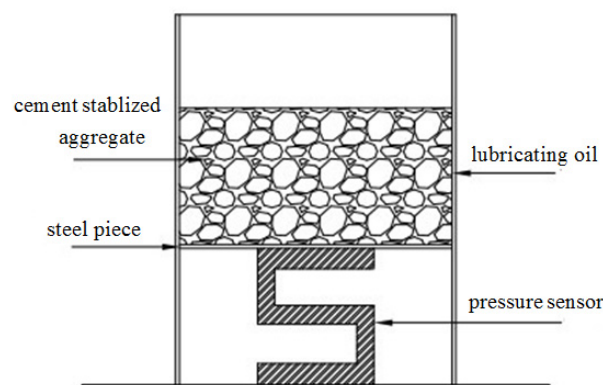


**Figure 4.** Compaction barrel and pressure sensor.

Compaction processes can be divided into three stages: the initial stage, the normal stage, and the stable stage. In the initial stage, the vibration pressure increases quickly from 0 to the set value, and the compaction parameters also increase rapidly. In the normal phase, the pressure and displacement are relatively stable, whereas the compaction degree increases slowly. In the stable phase, the parameters are fairly stable and the increase

in compaction degree is extremely slow. Three parallel experiments were carried out to determine the mean value and standard deviation of experiment results are analyzed below.

### 3. Results and Discussion

#### 3.1. Energy of Compaction Machine

The compaction-machine energy under 6 kind of working conditions, means different parameters(including the up/down weight number, eccentric block angle and frequency) combinations, was computed, and the results were presented in Table 2.

**Table 2.** Indoor vibration-compactor-energy calculation.

Working Conditions	1	2	3	4	5	6
Up counter Weight number	1	1	1	1	1	1
Up counter Weight number	3	3	3	3	3	3
Eccentric block angle/ $^{\circ}$	0	30	60	90	120	150
Frequency/(Hz)	28	28	28	28	28	28
Excitation force/N	6862.144	6630.955	5956.738	4888.691	3509.757	1959.144
Static eccentricity/(N $\times$ m)	0.22171	0.21424	0.19246	0.15795	0.11340	0.06330
$\varphi_0/^{\circ}$	409.117	399.315	373.8859	335.3064	274.3382	124.2212
$\varphi/^{\circ}$	423.364	414.069	390.355	355.515	303.099	183.761
$V/(m/s)$	0.46614	0.50815	0.57405	0.55873	0.38054	0.03919
$E/J$	22.429	27.63458	36.857	34.665	14.676	2.6043

According to Table 2, under general conditions, the maximum speed of the indoor vibratory compactor was about 0.6 m/s The total mechanical energy was about 40 J and common energy was in the range of 36 to 48 J.

#### 3.2. Transmitted Energy from Machinery to Material ( $E_t$ )

##### 3.2.1. First Two Cycles

The vibration-compaction parameters and hysteresis curves (VCPHC) of the two compaction during the initial stage are shown in Figure 5, which includes the time-history-displacement curve and force as well as the displacement-force hysteresis curve in each compaction process The energy transferred from the machine to the compacted material in one compaction process can be calculated by the displacement-force hysteresis curve of each compaction process The stored energy in the compacted material during a definite period could be defined by the overlapping area of multiple hysteresis curves.

Figure 5 shows the first two cycles The displacement and compaction pressure increased quickly The displacement increment of the two adjacent cycles was as high as 0.2 mm (shown as the displacement-time curve on the left top of Figure 5) if the material was loose and easy to compact. In this stage, the force-displacement hysteresis curve was not closely spaced and hardly overlapped. As mentioned in Section 2.2.3, three parallel experiments were carried out, and the  $\bar{A}_h$  (mean area value of hysteresis curve) was 305.9 N-mm,  $\sigma_{Ah}$  (the standard deviation of the hysteresis-curve area) was 23.25, and the increment of the hysteresis-curve-area value was nearly the same The force-displacement-curve area increased rapidly, which indicated that the energy absorbed by the compacted material increased quickly.

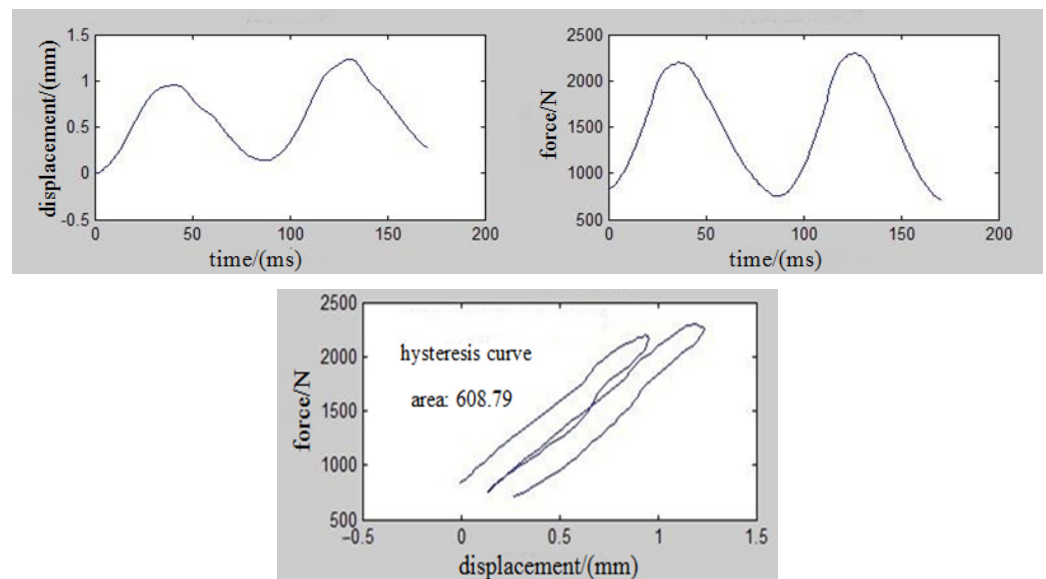


**Figure 5.** VCPHC of two cycles in initial stage.

### 3.2.2. Five Normal Cycles

Figure 6 shows the displacement, force, and hysteresis curves of five cycles in the normal compaction stage, in which the VCPHC parameters hardly changed under different compaction cycles. The displacement and force-signal curves were relatively close to the sine wave, and the value was stable. The displacement-force curves were all closed curves (highly coincident and dense) in these five cycles. Both the position and shape were identical and heavily overlapped. The hysteresis-curve area of one curve was about 1200 N·mm, which was significantly greater than the curve in the first two cycles. The area of the cumulative curve slightly increased compared to the single hysteresis curve. As the compaction continued, the hysteresis curves moved towards the right slowly. The coverage area of the displacement-force hysteresis curve increased gradually and slowly, which indicated that the energy absorbed by the compacted materials increased slowly.

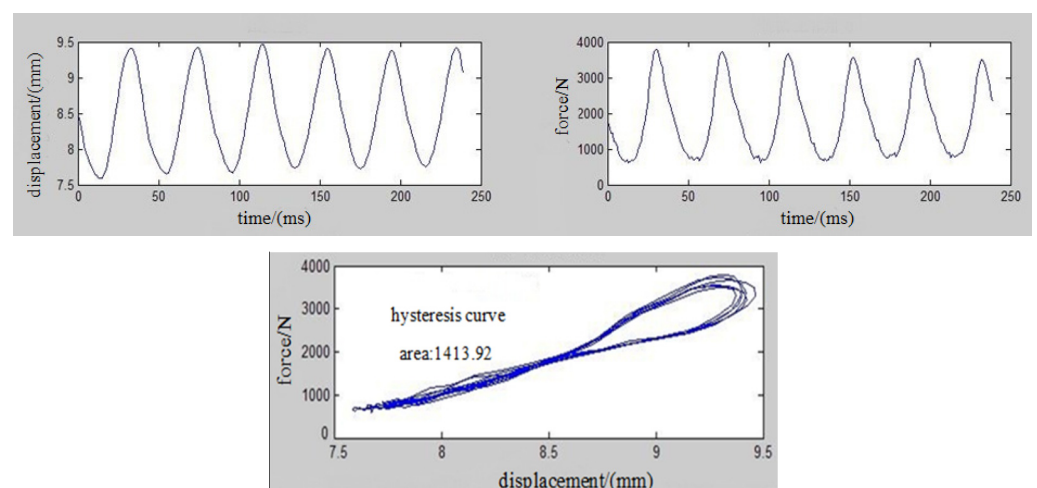


**Figure 6.** VCPHC of five cycles in normal stage.

In the stable stage, the compaction parameters were nearly fixed and the hysteresis curve [27] was nearly constant for a short time. Therefore, the hysteresis curve of this stage was not drawn.

### 3.2.3. Whole Compaction Process

Figure 7 shows the displacement, force, and hysteresis curves of the whole compaction, including 3 stages and the last 7 s. According to the force-displacement curve (Figure 7) and the hysteresis-curve-density degree, the compaction-hysteresis curve can be divided into three parts. The compaction hysteresis curve appearing during 0–1.5 s was the I stage or initial stage, in which the displacement fell between 0 and 4 mm. The hysteresis curve with 4–7.5 mm displacement was termed the II stage or normal stage, which appeared during the period from 1.5–4 s. The III stage, or dense stage, corresponded to the displacement of 7.5 mm and appeared after 4 s. These three hysteresis-curve-density stages corresponded to the three compaction stages.

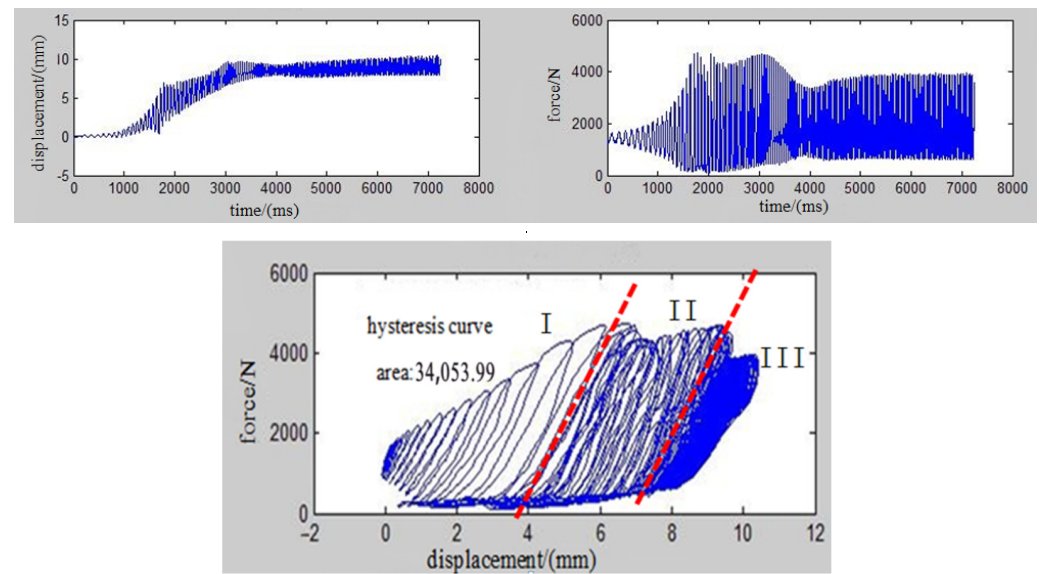
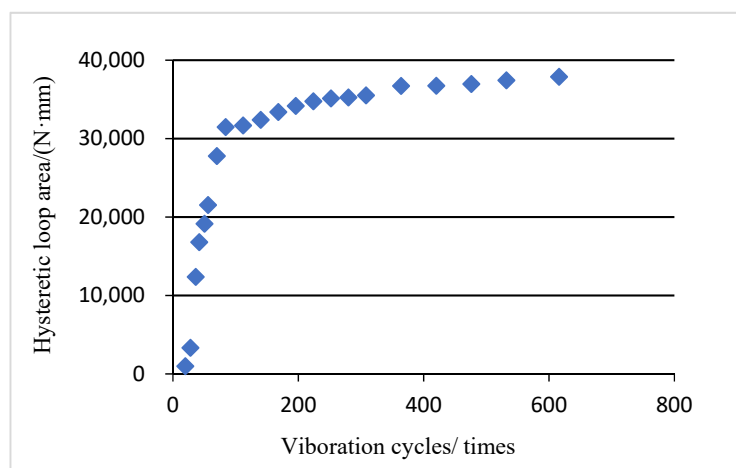


Figure 7. VCPHC of various stages.

According to the results of all the experiments, the  $\overline{A}_h$  (the mean area value of the hysteresis curve) was usually about 1200–1800 N·mm in the whole compaction stage, in addition to the initial stage. The duration of the initial stage was very short and the force was very low. As a result, the value of the energy in this stage can be. This indicates that the transit of mean energy to a compacted material in one compaction cycle is about 1.2–1.8 J. The vibration compaction lasted about 1 min and the common time range was half a minute to two minutes during the vibration-compaction processes. The energy transferred from the machine to the compacted material was about 2520 J and the common range was between 1260 and 5040 J. On this test, the compaction thickness was 7 cm. The standard energy can be estimated by thickness, and the energy must be about 5400 J. The common range is between 2700 and 10,080 J. The energy of heavy compaction (a kind of modified proctor compaction method used in China) is 5642 J. Heavy compaction and vibration compaction have similar energies (the compaction barrel volume of heavy compaction is slightly less than that of vibration compaction). The compaction effect of vibrate compaction is better as the internal friction angle of vibrating compacted material is lower for particle materials in the vibration state.

### 3.3. The Energy Stored by Compaction Materials $E_s$

The energy  $E_s$  can be described by the hysteresis-curve area. It increases during the compaction process. The relationship between  $E_s$  and the compaction cycle is shown in Figure 8.



**Figure 8.** Hysteresis-loop area of cement-stabilized aggregate.

The rising trend of the hysteretic curve area was close to the compaction-deformation curve. The  $\bar{A}_{hf}$  (the mean area value of the final hysteresis curve) was 38,046.3 N·mm, and the  $\sigma_{Ah}$  (the standard deviation of the final hysteresis-curve area) was 2411.17, which indicated that  $\bar{E}_s$  (the mean energy stored by the compacted cement-treated aggregate) was about 38 J. The hysteresis-curve area was nearly constant after 20 s. Therefore, the final area was only slightly affected by the compaction time.

The stored energy could also be computed by a simple physical method. The peak value of the compactor's mechanical excitation force was about 6000 N and the effective value of the compactor's excitation force was  $\frac{\sqrt{2}}{2}$  of the peak value; since the excitation-force curve was a sinusoid curve, the effective value of the compactor's excitation force was about 4200 N. At the initial stage, the compaction-vibration force increased from 0 to 6000 N and the compression displacement accounted for half of the whole compression displacement. The actual average effective value should be calculated as:  $(\frac{4200}{2} + 4200)/2 \approx 3200$  N. The compression displacement was at a distance of approximately 1 cm. Therefore, the work was about  $3200 \text{ N} \times 0.01 \text{ m} = 32 \text{ J}$ . The energy  $E_s$  value was determined to be 38 J according to the compaction experiment and 32 J according to the calculation methods. During one dynamic-compaction process, the cement-stabilized aggregate can absorb and save energy of about 32–38 J. The compaction volume was cylindrical: 15 cm in diameter and 7 cm thick.

### 3.4. The Analysis on Three Kinds of Energy

The energy  $E_{self}$  was about 40 J when it initiated the compaction of the material. However, for each compaction-contract process, the transmitted energy from machinery to compacted material ( $E_t$ ) was only 1–1.8 J. In a one-minute compaction process, about 2500 (2520) J of energy were transmitted, but only about 38 J could be stored and conserved by the material. The  $E_{self}$  was determined by the theoretical calculation and was unrelated to the specimen thickness. The  $E_t$  and  $E_s$  were measured by the actual experiment, which were affected by the compaction depth.

In this study, for the first time, the energy  $E_s$  value was defined by two different methods in indoor experiments.

## 4. Conclusions

- (1) In time order, compaction processes can be divided into three stages: the initial stage, the normal stage, and the stable stage. In compaction processes, the hysteresis curve of the three stages becomes more stable and dense, whereas the indenter-displacement speed becomes slow.

- (2) There are three kinds of energy in the vibration-compaction process: the mechanical energy itself ( $E_{self}$ ), the energy transmitted from the machinery to the compacted material ( $E_t$ ), and the energy stored by the compaction materials ( $E_s$ ), with energy values of 40 J, 2500 (2520) J, and 38 J, respectively.
- (3) In each compaction process, the energy transmitted from the machinery to the compacted material ( $E_t$ ) is only 1–1.8 J.

**Author Contributions:** Conceptualization, H.Z.; methodology, G.Z., Y.G.; software, H.Z.; validation, G.Z.; formal analysis, Q.X. and Z.W.; investigation, H.Z. and Y.G.; resources, H.Z.; data curation, G.Z.; writing—original draft preparation, Z.W.; writing—review and editing, G.Z. and Y.G.; visualization, H.Z.; supervision, H.Z. and Q.X.; project administration, H.Z. All authors have read and agreed to the published version of the manuscript.

**Funding:** This research received no external funding.

**Institutional Review Board Statement:** Not applicable.

**Informed Consent Statement:** Not applicable.

**Data Availability Statement:** The use of the data from this article requires permission from the author.

**Acknowledgments:** We express our sincere gratitude to the experts, teachers, and students who provided help for this paper.

**Conflicts of Interest:** The authors declare no conflict of interest.

## References

1. Wu, H. Study on Compaction Mechanism and Construction Technology of Highway Cohesive Soil Subgrade Filling. Master's Thesis, Fuzhou University, Fuzhou, China, 2020.
2. Feng, R.; Wang, Y.; Xie, Y. Test on Vibrated Compaction Properties of Coarse-grained Soil. *China J. Highw. Transp.* **2007**, *5*, 19–23.
3. Zhou, H.; Guo, Y.; Zhang, G. Study on relation between compaction energy and vibration compaction mechanical parameters. *J. Shandong Jianzhu Univ.* **2017**, *32*, 6.
4. Gurtug, Y.; Sridharan, A. Compaction behaviour and prediction of its characteristics of fine grained soils with particular reference to compaction energy. *Proc. Soc. Constr. Eng.* **2004**, *44*, 27–36. [[CrossRef](#)]
5. Hu, L. Study on Structural Types and Composition Design of Semi-Rigid Base Materials. Ph.D. Thesis, Chang'an University, Xi'an, China, 2004.
6. An, Z.; Liu, T.; Zhang, Q.; Zhang, Z.; Huangfu, Z.; Li, Q. Vibration compaction process model for rockfill materials considering viscoelastic-plastic deformation. *Autom. Constr.* **2021**, *131*, 103889. [[CrossRef](#)]
7. Bratu, P.; Dobrescu, C. Dynamic response of Zener-modelled linearly viscoelastic systems under harmonic excitation. *Symmetry* **2019**, *11*, 1050. [[CrossRef](#)]
8. Paulmichl, I.; Furtmueller, T.; Adam, C.; Adam, D. Numerical simulation of the compaction effect and the dynamic response of an oscillation roller based on a hypoplastic soil model. *Soil Dyn. Earthq. Eng.* **2020**, *132*, 106057. [[CrossRef](#)]
9. Wang, M.; Yu, Q.; Xiao, Y. Experimental investigation of macro- and meso-scale compaction characteristics of unbound permeable base materials. *Chin. J. Rock Mech. Eng.* **2022**. *network preprint*.
10. Wang, N. Numerical Simulation and Mechanical Analysis of High Filling Embankment Construction Method. Master's Thesis, Chongqing Jiaotong University, Chongqing, China, 2019.
11. Jia, J.; Yang, X.; Liu, H. Compaction Characteristics of Paver Tamper to Mixture Considering Shock Load. *J. Southwest Jiaotong Univ.* **2022**. *network preprint*.
12. Massarsch, K.R.; Fellenius, B.H. Evaluation of Vibratory Compaction by In Situ Tests. *J. Geotech. Geoenviron. Eng.* **2019**, *145*, 05019012. [[CrossRef](#)]
13. Jiao, G.D.; Zhao, S.P.; Ma, W.; Kong, X.B. Evolution laws of hysteresis loops of frozen soil under cyclic loading. *Chin. J. Geotech. Eng.* **2013**, *35*, 1343–1349.
14. Aloisio, A.; Alaggio, R.; Köhler, J.; Fragiaco, M. Extension of Generalized Bouc-Wen Hysteresis Modeling of Wood Joints and Structural Systems. *J. Eng. Mech.* **2020**, *146*, 04020001. [[CrossRef](#)]
15. Triantafyllidis, T.; Kimmig, I. A simplified model for vibro compaction of granular soils. *Soil Dyn. Earthq. Eng.* **2019**, *122*, 261–273. [[CrossRef](#)]
16. Cao, Z. Road Engineering Properties of Metamorphic Soft Rock used as Embankment Filling in Qin-Ba Mountain Areas and Vibration Compaction Technology Research. Ph.D. Thesis, Chang'an University, Xi'an, China, 2013. (In Chinese).
17. Liu, D.; Li, Z.; Liu, J. Experimental study on real-time control of roller compacted concrete dam compaction quality using unit compaction energy indices. *Constr. Build. Mater.* **2015**, *96*, 567–575. [[CrossRef](#)]

18. Ye, Y.; Cai, D.; Zhu, H.; Wei, S.; Yang, W.; Gen, L. Research on the continuous inspection and control index of new high speed railway subgrade compaction based on vibration energy. *Tiedao Xuebao/J. China Railw. Soc.* **2020**, *42*, 127–132. (In Chinese)
19. Yang, C.; Zhang, L.; Su, K. Research on dynamic response of railway subgrade filling material under vibration compaction based on VMD-Hilbert transform. *Yanshilixue Yu Gongcheng Xuebao/Chin. J. Rock Mech. Eng.* **2022**, *41*, 2991–3001.
20. Susante, P.V.; Mooney, M.A. Capturing nonlinear vibratory roller compactor behavior through lumped parameter modeling. *J. Eng. Mech.* **2008**, *134*, 684–693. [[CrossRef](#)]
21. Javier, G.C.; Daniel, G.V.; Jaime, D. Nonlinear modelling and simulation of vibrocompaction processes. *Int. J. Non-Linear Mech.* **2018**, *102*, 101–111.
22. Imran, S.A.; Barman, M.; Nazari, M.; Commuri, S.; Zaman, M.; Singh, D. Continuous monitoring of subgrade stiffness during compaction. *Transp. Res. Procedia* **2016**, *17*, 617–625. [[CrossRef](#)]
23. Wang, L. Evaluation of vibratory compaction capacity and compactability of road base materials. *J. Tongji Univ. (Nat. Sci. Ed.)* **2013**, *41*, 203–207.
24. Pan, L. Study on Quality Control of Cement Stabilized Macadam Base under Vertical Vibration Compaction. Master's Thesis, Hebei University, Baoding, China, 2021.
25. Su, G. Study on Vibration Forming Test and Application of Cement Stabilized Macadam. Master's Thesis, South China University of Technology, Guangzhou, China, 2018.
26. Kloubert, H.J.; Americas, B. Intelligent Soil and Asphalt Compaction Technology. In Proceedings of the 85th TRB Annual Meeting, Washington, DC, USA, 22–26 January 2006; pp. 1–10.
27. Massarsch, K.R. Effects of Vibratory Compaction. TransVib 2002. International Conference on Vibratory Pile Driving and Deep Soil Compaction. Louvain-la-Neuve. Keynote Lecture. 2002, pp. 33–42. Available online: [https://www.researchgate.net/publication/292792536\\_Effects\\_of\\_vibratory\\_compaction](https://www.researchgate.net/publication/292792536_Effects_of_vibratory_compaction); <https://www.researchgate.net/publication/292792536> (accessed on 7 September 2022).